SACLANTCEN REPORT
serial no: SR-276

SACLANT UNDERSEA RESEARCH CENTRE REPORT

MODELLING OF SCATTERING BY OBJECTS ON THE SEABED

J.A. Fawcett, W.L.J. Fox, A. Maguer

October 1997

The SACLANT Undersea Research Centre provides the Supreme Allied Commander Atlantic (SACLANT) with scientific and technical assistance under the terms of its NATO charter, which entered into force on 1 February 1963. Without prejudice to this main task – and under the policy direction of SACLANT – the Centre also renders scientific and technical assistance to the individual NATO nations.

This document is approved for public release.
Distribution is unlimited

SACLANT Undersea Research Centre
Viale San Bartolomeo 400
19138 San Bartolomeo (SP), Italy

tel: +39-187-540.111
fax: +39-187-524.600

e-mail: library@saclantc.nato.int

NORTH ATLANTIC TREATY ORGANIZATION

Modelling of scattering by objects on the seabed

J.A. Fawcett, W.L.J. Fox, and A. Maguer

The content of this document pertains to work performed under Project 033-3 and Project 031-2 of the SACLANTCEN Programme of Work. The document has been approved for release by The Director, SACLANTCEN.

Director

intentionally blank page

Modelling of scattering by objects on the seabed

J.A. Fawcett, W.L.J. Fox, and A. Maguer

Executive Summary:

A better understanding of the scattering of acoustic energy from objects on the seabed will lead to a significant improvement in our ability to detect and classify minelike objects. The seabed will reflect the incident pulse and hence the energy incident upon the object is a combination of the original and the reflected version of the pulse. Similarly, the scattered energy received at a hydrophone in the water is a combination of totally water-borne and bottom-interacting energy. The effect of the seabed can thus have a significant effect upon the resulting amplitude and shape of the received backscattered signal.

This paper describes some of the theory and implementation issues concerned with modelling scattering from cylindrical or spherical objects lying on the seabed. The model is then used to investigate the effects of various parameters such as grazing angle of the incident energy, receiver/scatterer geometry, and the bottom halfspace geoacoustic parameters. The paper is concluded with a comparison of modelled time series with experimental scattering data obtained for a steel-shelled cylinder and a solid aluminum sphere lying on a sandy seabed.

In the future we would like to continue the studies of this paper for the case when the objects are partially or totally buried. It would also be useful to extend the modelling to allow for seabed roughness.

intentionally blank page

Modelling of scattering by objects on the seabed

J.A. Fawcett, W.L.J. Fox, and A. Maguer

Abstract:

This paper describes some of the theory and implementation issues of modelling the backscattered energy from cylindrical or spherical objects lying on the seabed. The model utilizes a single-scatter approximation. The effects of various parameters such as grazing angle of the incident energy, receiver/scatterer geometry and the bottom halfspace geoacoustic parameters are investigated numerically. The paper is concluded with a comparison of modelled time series with experimental scattering data obtained for a steel-shelled cylinder and a solid aluminum sphere lying on a sandy seabed.

Keywords: Cylinder, sphere, seabed, scattering

Contents

1

Introduction

When a scattering object is near an interface, the interface will modify the field incident upon the object and will also modify the field scattered by the object. There are, in fact, an infinite sequence of interactions between the object and the interface. The "single-scatter " approximation (SSA) is achieved by modelling the scattering from the object as a free-space scattering process and including the effects of the interface on modelling the incident field and the propagation of the scattered field; only single scatterings from the object are modelled. This type of approximation has been used by other authors (e.g., [1],[2]) for object/waveguide scattering problems. For the case of an object lying on the seabed we expect this approximation to be accurate for the specular reflection. However, it is not clear that this approximation will properly describe the effect of the seabed on energy which propagates circumferentially about the object. One would expect that the character of the circumferential waves could be changed along the portion of the object on or very close to the seabed. There are methods which model all the interactions between the scattering object and the interface for proud, buried, or partially buried objects [3]-[7] but these methods are more computationally intensive and we expect the SSA to accurately model the specular portion of the scattered signal (and hope that it adequately models the remainder of the signal).

We will outline the theory used for the computation of scattering from cylinders and spheres lying on the seabed. We will show in the temporal domain how the interface changes the nature of the signal backscattered by the object. Finally, we compare our model results (both in the spectral and temporal domains) with experimental data obtained from a water-filled cylindrical shell and for an aluminum sphere lying on the sea bottom.

2
Theory

Solutions for scattering from cylinders and spheres in free space are most readily constructed in terms of the appropriate special functions; radial Bessel/Hankel functions with azimuthal trigonometric functions in the case of the cylinder and spherical Bessel/Hankel functions with spherical harmonic functions in the case of scattering from a sphere. However, the modelling of propagation in a two halfspace environment is most easily described in terms of wavefunctions with vertical and radial dependencies. Thus the functions which most easily describe the propagation process are not the same as those which most easily describe the scattering process. In order to compute the scattering solutions for an object near an interface, it will be neccessary to be able to express the functions of the one representation in terms of the other. Below, we outline the necessary transformations for the two-dimensional infinite cylinder case and for the three-dimensional spherical case.

2.1 Incident Field

We take the source to be sufficiently distant from the cylinder or sphere that the incident field can be approximated as direct and interface-reflected plane-waves (see Fig. 1 below). Thus we can consider the incident field to have the form

$$\begin{aligned} p^{inc} &= \exp(i\frac{\omega}{c}[z\cos\phi_{inc} + x\sin\phi_{inc}]) \\ &+ R^{inc}(\omega,\phi_{inc})\exp(-2ia\frac{\omega}{c}\cos\phi_{inc})\exp(i\frac{\omega}{c}[z\cos\phi_{inc} + x\sin\phi_{inc}]) \end{aligned} \quad (1)$$

where $R^{inc}(\omega,\phi_{inc})$ is the plane-wave reflection coefficient, a is the radius of the cylinder or sphere and $\exp(-2ia\omega/c\cos\phi_{inc})$ accounts for the phase difference between the direct and reflected wavefronts (it should be noted that because of our definition of ϕ_{inc}, $\cos\phi_{inc}$ is negative). It is straightforward, by using a distribution of generalized plane waves of the form of Eq.(1), to generate more general incident fields.

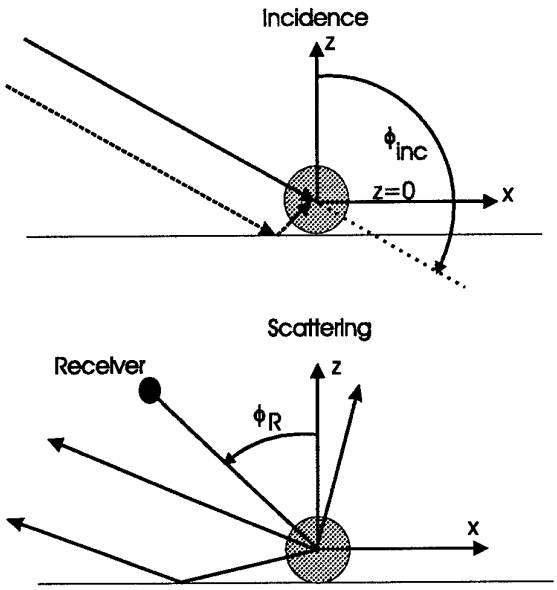

Figure 1: *Schematic of incident and scattering geometry*

2.2 Scattered field

We first consider the form of the scattered fields for the cylinder and sphere in free space. The effect of the seabed on the propagation of these fields will be subsequently included. For the infinite cylinder we can express the scattered field for a broadside geometry in the form [8],

$$p^{sc}(r, \phi_R; \phi_{inc}) = \sum_{m=0}^{N} t_m H_m(kr) \cos(m(\phi_R - \phi_{inc})). \tag{2}$$

The angle, ϕ_R, as shown in Fig. 1 must be taken with a negative sign when measured in a counter-clockwise direction. The scattering coefficients t_m can be determined in a straightforward fashion (numerical parameters associated with the incident plane-wave are included in our definition of t_m) using separation of variables. Thus, the scattered field for the incident field of the form of Eq.(1) is

$$\begin{aligned} p^{sc} &= \sum_{m=0}^{N} t_m H_m(kr)[\cos(m(\phi_R - \phi_{inc})) \\ &+ R^{inc} \exp(-2ia\frac{\omega}{c}\cos(\phi_{inc}))\cos(m(\phi_R + \phi_{inc} - \pi))] \end{aligned} \tag{3}$$

where H_m denotes the Hankel function of the first kind.

Similarly, for a spherical shell we can write

$$p^{sc} = \sum_{n=0}^{N} \sum_{m=0}^{n} t_n h_n(kr)[P_n^m(\cos(\phi_{inc}))P_n^m(\cos\phi_R) + R^{inc}\exp(-2ia\frac{\omega}{c}\cos\phi_{inc})P_n^m(\cos(\pi-\phi_{inc}))P_n^m(\cos\phi_R)]\cos m(\beta-\beta_{inc}) \quad (4)$$

where P_n^m are the Legendre polynomials, h_n are the spherical Hankel functions and β is the angle in the horizontal plane; we will take $\beta - \beta_{inc} = \pi$ in our computations.

2.3 Propagation of scattered field

Above, expressions for the scattered field in the immediate vicinity of an infinite cylindrical shell, Eq.(2), and in the vicinity of a spherical shell Eq.(4), are given. Now, in order to propagate these scattered fields to a specified receiver location, we must express the angular/radial functions in terms of vertical plane-wave components. The plane-wave component expression can then be modified to include the effect of the water/basement interface.

Infinite cylinder

For the cylinder, we wish to express functions of the form $H_m(kr)\cos m(\phi_R - \phi_{inc})$ in terms of plane waves. It is possible to write for $z > 0$ (following the plane-wave expansion of, for example, [8]),

$$H_m(kr)\cos m(\phi_R - \phi_{inc}) = \frac{e^{-im\pi/2}}{\pi}\int_{-\infty}^{\infty}\frac{e^{i(k_x x_R + \gamma z_R)}}{\gamma}\cos m(\psi - \phi_{inc})dk_x \quad (5)$$

and for $z < 0$

$$H_m(kr)\cos m(\phi_R - \phi_{inc}) = \frac{e^{+im\pi/2}}{\pi}\int_{-\infty}^{\infty}\frac{e^{i(k_x x_R - \gamma z_R)}}{\gamma}\cos m(\psi + \phi_{inc})dk_x \quad (6)$$

where $\psi \equiv \sin^{-1}(k_x c/\omega)$ and $\gamma \equiv \sqrt{\omega^2/c^2 - k_x^2}$. The angle ϕ_R implicitly enters Eqs.(5) and (6) through the Cartesian coordinates x_R and z_R which correspond to a range of r and an angle of ϕ_R. In order to account for the bottom interface we modify the plane-wave expression for the function of Eqs.(5) and (6), yielding the new function

$$C_m^{sc}(x,z,\phi_{inc}) \equiv \int_{-\infty}^{\infty}\frac{e^{i(k_x x+\gamma z)}}{\gamma}[\frac{e^{-im\pi/2}}{\pi}\cos m(\phi_{inc}-\psi) + R(k_x)\frac{e^{+im\pi/2}}{\pi}\cos m(\phi_{inc}+\psi)e^{2i\gamma a}]dk_x. \quad (7)$$

where $R(k_x)$ is the plane-wave reflection coefficient for the horizontal wavenumber k_x. In Eq.(3) we replace $H_m(kr)\cos m(\phi_R + \phi_{inc} - \pi)$ and $H_m(kr)\cos m(\phi_R - \phi_{inc})$ by the expressions of the form of Eq.(7), yielding

$$\begin{aligned} p^{sc} &= \sum_{m=0}^{N} t_m [C_m^{sc}(x_R, z_R, \phi_{inc}) \\ &+ R^{inc} \exp(-2ia\omega/c \cos\phi_{inc}) C_m^{sc}(x_R, z_R, \pi - \phi_{inc})]. \end{aligned} \tag{8}$$

Spherical shell

In the spherical case, we wish to express $h_n(kr)P_n^m(\cos\phi)$ in terms of vertical plane waves. Following [3], it is possible to write for $z > 0$,

$$h_n(kr)P_n^m(\cos\phi) = i^{m-n} \int_0^\infty \frac{pJ_m(p\zeta)e^{+i\gamma z}}{k\gamma} P_n^m(\frac{-\gamma}{k})dp \tag{9}$$

and for $z < 0$

$$h_n(kr)P_n^m(\cos\phi) = i^{m-n} \int_0^\infty \frac{pJ_m(p\zeta)e^{-i\gamma z}}{k\gamma} P_n^m(\frac{+\gamma}{k})dp \tag{10}$$

where ζ is the cylindrical radial value of the receiver and $\gamma \equiv \sqrt{k^2 - p^2}$. As with the cylinder we can modify $h_n(kr)P_n^m(\cos\phi)$ to account for the effect of the water/basement interface, yielding

$$S_{m,n}^{sc}(\zeta, z) \equiv i^{m-n} \int_0^\infty \frac{[P_n^m(\frac{-\gamma}{k}) + e^{2i\gamma a} P_n^m(\frac{\gamma}{k})R(p)]J_m(p\zeta)e^{i\gamma z}}{k\gamma} p\, dp. \tag{11}$$

Using this expression in Eq.(4) we can write for the spherical shell,

$$\begin{aligned} p^{sc} &= \sum_{n=0}^{N} \sum_{m=0}^{n} t_n S_{m,n}^{sc}(\zeta, z)[P_n^m(\cos(\pi - \phi_{inc})) + \\ \times\ & R^{inc} \exp(2ia\omega/c \cos\phi_{inc}) P_n^m(\cos\phi_{inc})] \cos m(\beta - \beta_{inc}). \end{aligned} \tag{12}$$

3

Numerical simulations

We will consider two basic cases; a generalized plane-wave (i.e., the direct and reflected planewaves coherently combined) incident upon an infinite cylindrical shell resting on the oceanic bottom and a generalized planewave incident upon a sphere resting on the bottom. For the infinite cylinder the broadside geometry is considered. The numerical approach is basically the same in the two cases; we compute the free-space scattering coefficients t_m using standard separation-of-variables techniques. The integrals for C_m^{sc} or $S_{m,n}^{sc}$ are numerically evaluated using numerical quadrature. In order to compute time domain signals, we compute the scattered signal at a receiver as a function of frequency and then Fourier synthesize the time domain signal. The Ricker wavelet which is used as the incident pulse in the simulations is shown in Fig. 2 and its power spectrum in Fig. 3.

3.1 *Water-filled cylindrical shell*

In this first example we consider a 6mm-thick steel-shelled cylinder of radius 0.25m. The interior of the cylinder is taken to be filled with water. The cylinder lies on a sandy bottom for which we use the parameters: C_p = 1710 m/s, $\rho = 1800 kg/m^3$ and we take the shear speed to be zero. The sound speed in the water was taken to be 1510 m/s. For the first set of curves shown in Fig. 4 we take the grazing angle to be fixed at 3° and then vary the angle of the receiver with respect to the cylinder centre from 3° to 12° in steps of 1.5° [in Fig. 1 we showed an angle of incidence, ϕ_{inc} measured off the vertical axis; for the remainder of this report, angles will be measured off the horizontal axis]. The range of the receiver is fixed at 7.5 m. The curves have been normalized by the maximum amplitude of the first curve. As can be seen the specular reflection portion of the time series shows the most variation. For the range of angles considered in the computations there is a widening of the specular pulse until about 10.5° at which point the specular reflections propagating along the direct and interface reflected paths begin to become distinguishable. There is a slight increase in amplitude going from the first to second curve and then the amplitude of the specular portion of the signal steadily decreases.

For the curves of Fig. 5 we consider the receiver angle to be fixed at 3° and vary the angle of incidence from 3° to 12° as above for the receiver angle. There are similar features as when varying the receiver angle; the specular pulse widens for larger

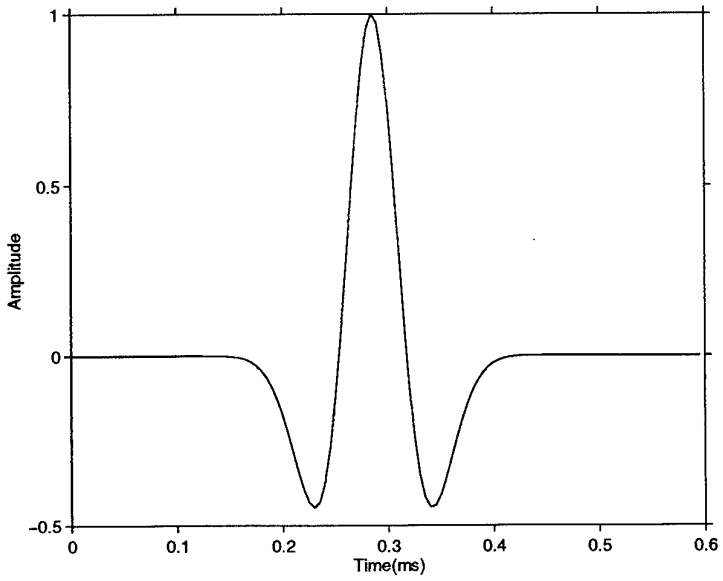

Figure 2: *Source wavelet used in computations*

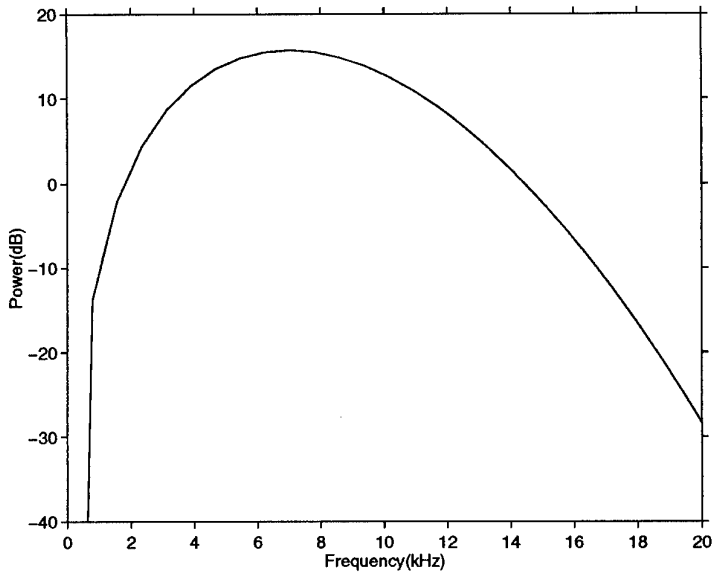

Figure 3: *Power spectrum of source wavelet used in computations*

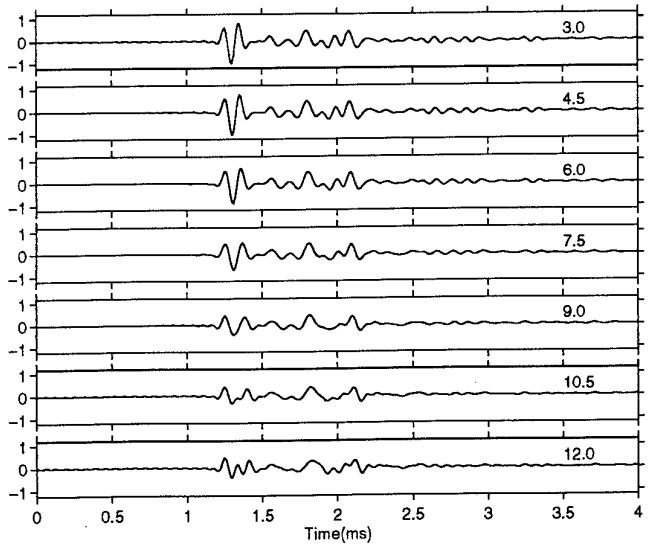

Figure 4: *Variation of backscattered time series as a function of receiver angle for an angle of incidence of 3°*

offset angles and there is an increased amplitude at the smaller angles. From the two sets of curves we can see that varying the incidence angle and receiver angles between 3 and 7.5° the overall amplitude of the signal can be changed but the shape of the signals is essentially the same. The features in the time series which come after the specular reflection are due to a combination of circumferential energy and energy which enters into the water of the cylinder and reflects back off the back face of the shell.

We now fix the angle of incidence and the receiver angle to be 4.5° and consider variations of the bottom sediment. The sediment properties are varied in the following fashion: $c_{sed} = 1510 + (j-1) \times 60$ m/s and the corresponding densities are given by $\rho = 1.0 + (j-1) \times .2$ g/cm^3. The resulting time series are shown in Fig. 6; the first curve is the free space result as there is no interface contrast in this case. The curves have all been normalized to the peak amplitude of the first curve. It can be seen that there is a large increase in amplitude (approximately a factor of 4) in going from curve 1 to curve 2 and the shape of the specular reflection has also changed. There is a slight change in the specular reflection going to the third curve and then there is very little variation.

We now repeat the above computations keeping the sediment density fixed at 1.0 g/cm^3 and varying the sediment sound speed $c_{sed} = 1510 + (j-1) \times 10$ m/s. The resulting normalized time series are shown in Fig. 7. There is a doubling of amplitude in going from the first curve (free space result) to the second curve with only a 10 m/s sound speed jump at the bottom. Over the subsequent curves there is a slower

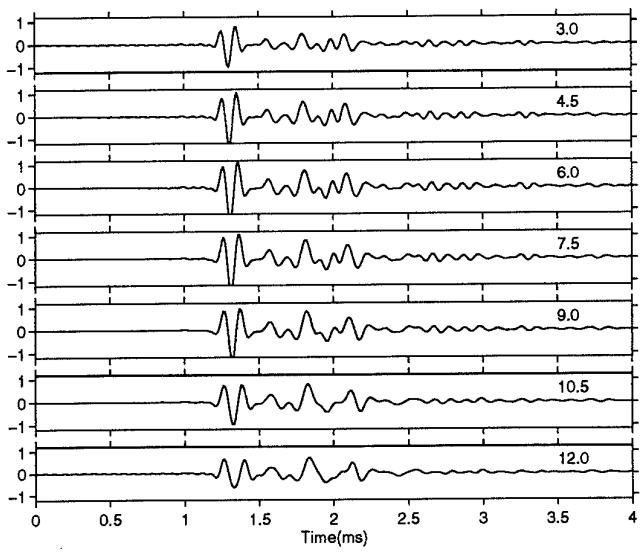

Figure 5: *Variation of backscattered time series as a function of incidence angle for a fixed receiver angle of 3°*

increase in amplitude and an increase in the amplitude of the second positive peak in the specularly reflected pulse (i.e., the shape of the specular reflection changes).

We have shown in these last two numerical simulations that for low grazing angles (both for the incident energy and the angle of the receiver with respect to the scatterer) the scattering of energy off the bottom interface can increase the backscattered levels significantly from the free-space results. Also the shape of the specular reflection is changed as a consequence of the coherent interference between direct and bottom reflected energy. For low grazing angles, the backscattered signal is almost invariant to the sediment parameters except for sound speeds very close to the water value. This is because a small grazing angle becomes subcritical for only a small sound speed contrast at the bottom. After the angles of incidence and the receiver angle are subcritical, the bottom characteristics have a very small effect on the reflection processes in the water column. The dependence of the backscattering from the cylinder on the sediment density is very weak. These results are for a particular incident pulse and cylinder radius. We would expect that for a fixed geometry, the totally water-borne and bottom interacting energy would become increasingly resolvable in the time domain for higher frequency pulses or for larger cylinder radii.

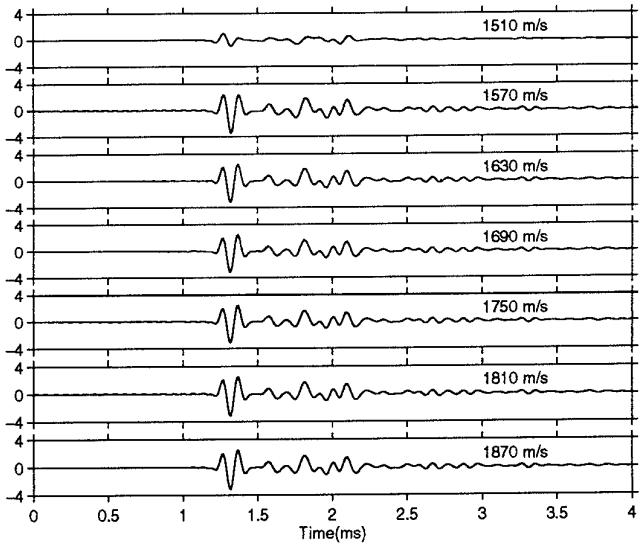

Figure 6: *Variation of backscattered time series from cylinder as a function of bottom sediment properties*

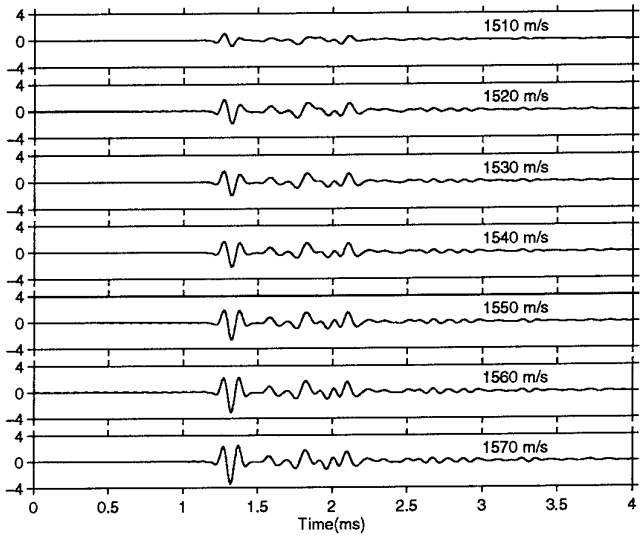

Figure 7: *Variation of backscattered time series from cylinder as a function of bottom sediment properties: fine variation*

3.2 Solid aluminum sphere

We now repeat the numerical simulations of the previous subsection but for a 0.3 m radius, solid aluminum sphere. For the sphere we use the values $c_p = 6380$ m/s, $c_s = 3100$ m/s and $\rho = 2790$ kg/m^3. The bottom sediment has the parameters of the previous subsection. In Fig. 8 we show the backscattered time series for a fixed angle of incidence of 3° and for the angle of the receiver varied, and in Fig. 9 for a fixed receiver angle of 3° and a variable angle of incidence.

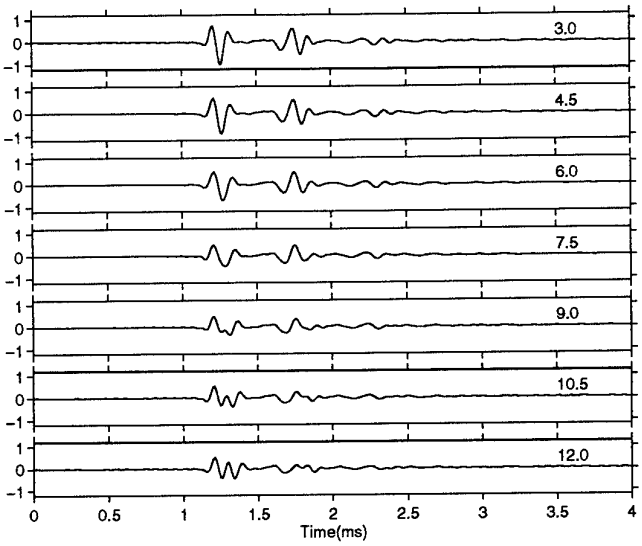

Figure 8: *Variation of backscattered time series from sphere as a function of receiver angle for an angle of incidence of 3°*

The trends of these two figures are the same as in the cylinder case - there is a widening of the specularly-reflected pulse with increasing angles - for the case of varying the receiver angle, the direct and reflected portions of the specularly-reflected pulses start to be distinct in the time domain. There is also a variation in amplitude of the backscattered signal with respect to angle. An interesting feature of the backscattered signal from the aluminum sphere is that for these low incidence and receiver angles, the reflected pulse "appears" to be the negative of the source pulse. This is the opposite of what one would expect in free space. Thus, in this case, the presence of the bottom interface has dramatically changed the character of the specularly reflected pulse. The second pulse which is evident in the time series is a wave which has travelled circumferentially around the sphere - this particular wave is referred to as the Rayleigh wave in the scattering literature [9].

We now examine the variation of the backscattered time series as a function of the bottom sediment. We use the same sets of sediments as in the study of the

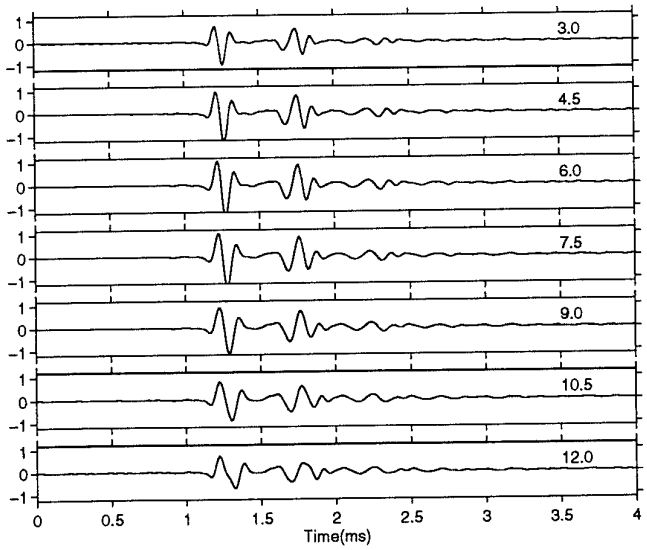

Figure 9: *Variation of backscattered time series as a function of angle of incidence for a receiver angle of 3°*

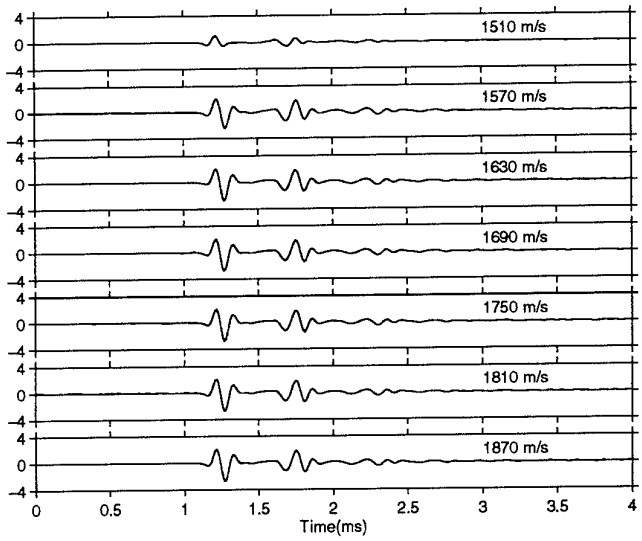

Figure 10: *Variation of backscattered time series from aluminum sphere as a function of bottom sediment properties*

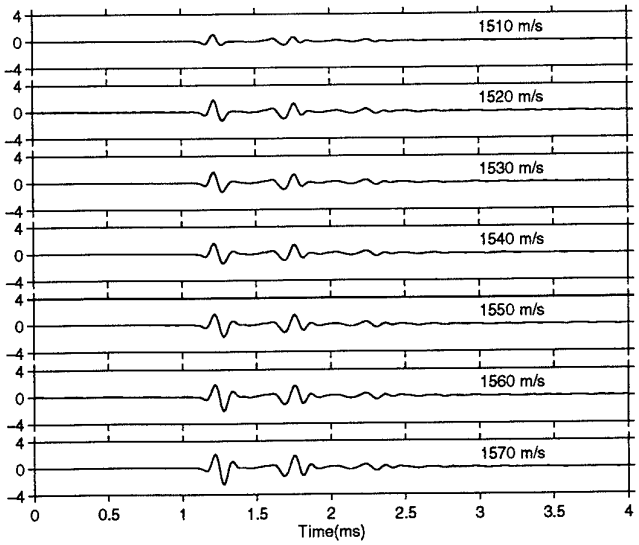

Figure 11: *Variation of backscattered time series from aluminum sphere as a function of bottom sediment properties: fine variation*

water-filled cylinder. The resulting sets of time series are shown below in Figs. 10 and 11. As with the cylinder, the presence of the seabed significantly increases the backscattered amplitude from the free space results (the first curves in Figs. 10 and 11). In Fig. 11 the gradual transition of the specular pulse shape due to the seabed can be seen. This set of curves illustrates that, in fact, the specularly-reflected pulse for the seabed case is not the negative of that for the free-space case. There is a gradual change in the features of the this pulse, such that the resulting pulse of the last curves seems to be the negative of the free space pulse when shifted by a fraction of a millisecond.

4

Real data examples

During October/November 1996 the SACLANTCEN Mine Countermeasures Group performed sonar/object scattering measurements near the island of Elba. We will consider data obtained for a water-filled cylinder and a solid aluminum sphere lying on a sandy bottom. A parametric source, the TOPAS 110] sonar transmitter, was mounted on a 3.7m high tower and was typically 40-50m away from the scattering object. This resulted in an effective grazing angle of approximately 4°. A receiving hydrophone was positioned 6-7.5 m in front of the object by a diver; this hydrophone is very approximately along an imaginary line from the object to the top of the TOPAS tower (see Fig. 12). The same type of experiment setup was used for free-field measurements described in [11].

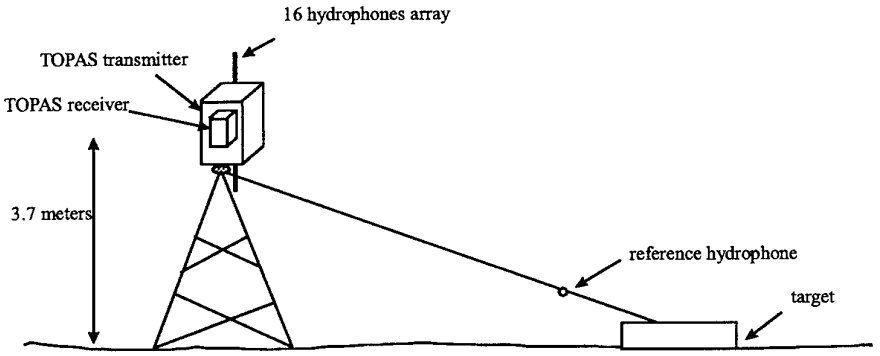

Figure 12: *Schematic of scattering geometry used during experiments*

4.1 Water-filled cylinder

The cylindrical shell used in these experiments is the same as that used in previous scattering experiments [11]. It is 2m long and has a radius of 0.25m. The shell is steel and is 6mm thick. The cylinder is filled with water. We consider the cylinder when it is in the broadside position with respect to the receiver and incident beam. The finite cylinder is modelled as an infinitely long cylinder; this is a good approximation for the frequencies and receiver range of this experiment [11]. The source pulse was

approximately that of Figs. 2 and 3 - however, instead of explicitly modelling the source, a recorded direct arrival pulse shape from the experiment of [11] was used. We did not use the recorded incident pulses from the present experiment because these pulses seemed to often include some bottom-reflected energy. For the data shown below the TOPAS array was located 44.5m away from the cylinder.

In general, there is uncertainty with respect to some of the details of the experimental geometry. The receiver (reference) hydrophone was aligned between the source and target by having divers run a line from the tower to the target and suspending the hydrophone from this line. Even with this system, there may not have been perfect alignment between the source, hydrophone, and target due to slack in the line and currents in the water. The TOPAS beam (which has a beamwidth of approximately $\pm 2.5°$) may have not been perfectly aligned with the imaginary line between the hydrophone and object centre. Because of these geometrical uncertainties, it was decided to compare normalized data and model time series (i.e., the absolute amplitude of the backscattered signal is not modelled).

We assume that the hydrophone was located at an angle of 4° with respect to the cylinder centre and at a range of 7.5m. We will take the bottom to have a compressional velocity of 1710 m/s and a density of 1800 kg/m^3. In Fig. 13 we plot the recorded time series for the TOPAS beam oriented at a grazing angle of 3.5°. The amplitude of the time series has been normalized by its peak amplitude. There were other time series for this site and although they are all fairly similar, there was some experimental variation in the details of the specular reflection.

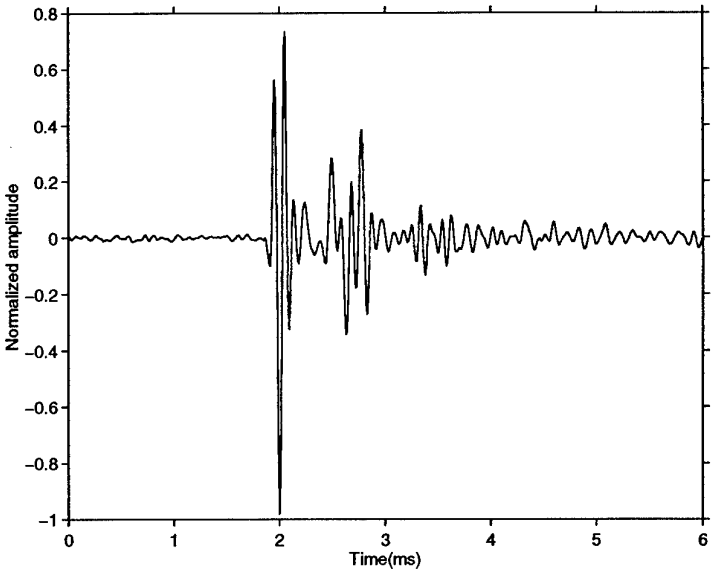

Figure 13: *Time series for backscatter from cylinder*

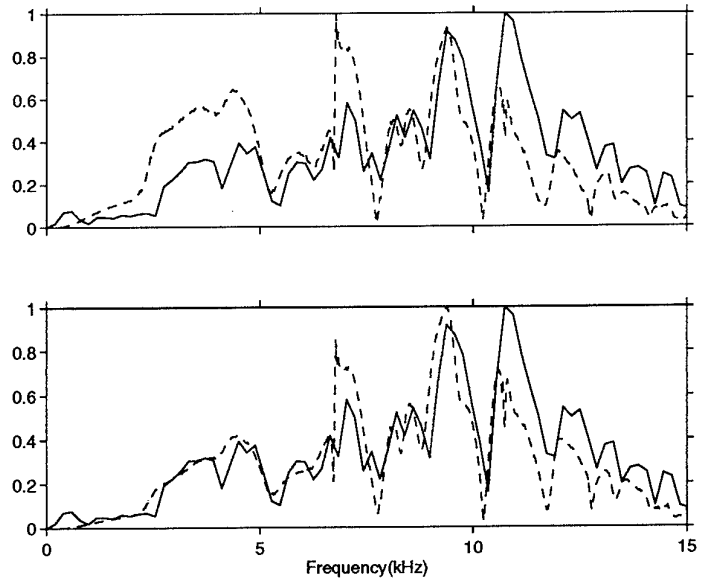

Figure 14: *Comparison of experimental(solid) and modelled(dashed) spectra for (a) free space model (b) single-scatter model*

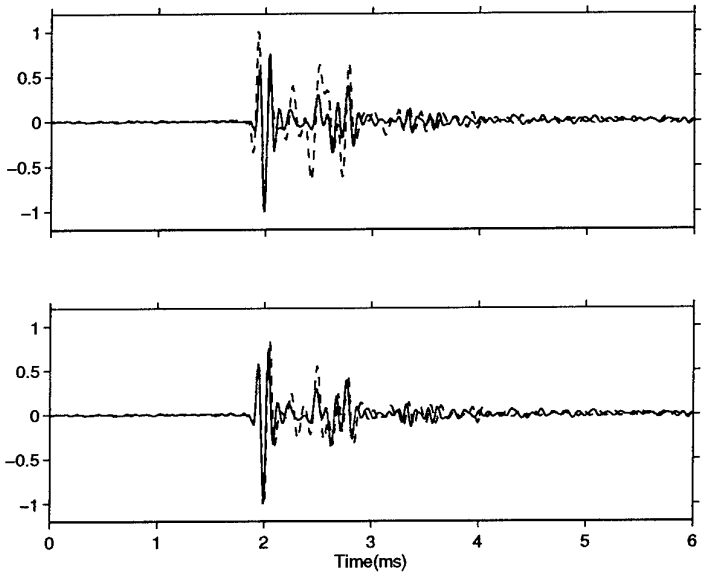

Figure 15: *Comparison of experimental(solid) and modelled time series(dashed) for (a) free space model (b) single-scatter model*

In Fig. 14 we show the spectrum of the energy for the angle of incidence equal to 3.5° (solid line) and the resulting model spectra using: (1) a homogeneous free space model (in fact, we use the SSA model with zero impedance jump at the bottom) (2) the SSA model for the seabed. The free space model correctly predicts the features of the spectrum but does not exhibit the correct amplitude trend. The SSA model is in better agreement, although there is still a difference in levels for the higher frequencies.

In Fig. 15 we show a similar comparison in the time domain. The modelled and experimental time series are positioned with respect to each other by aligning the positions of their maximum peak amplitudes (the maximum absolute values). In this case, the SSA has not only correctly modelled the specular portion of the backscattered signal but has also modelled the rest of the time series very well. As mentioned previously, it is not clear how well the SSA will do in modelling circumferential energy. It is evident that the SSA model has done a better job than a free space model in predicting the backscattered signal. In Fig. 16 we show a "zoomed-in" comparison between the specular reflected pulses as predicted in free space and by the SSA.

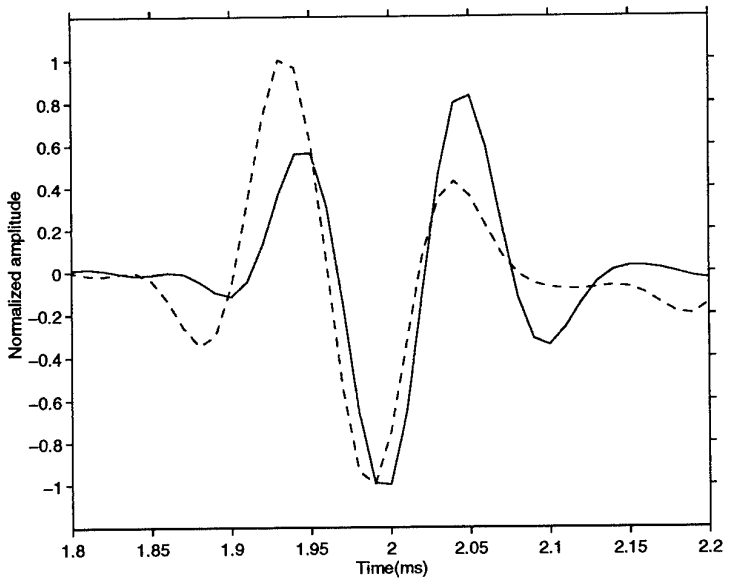

Figure 16: *Comparison of specularly reflected pulse as computed by single-scatter model (solid line) and free space model (dashed line)*

4.2 Aluminum sphere

The aluminum sphere used in the experiments had a radius of 0.3 m. We use the following parameters for aluminum c_p = 6380 m/s, c_s = 3100 m/s and ρ = 2790 kg/m^3.

In Fig. 17 we show two experimental time series (normalized to have unity peak amplitude). These time series are from two different days, sites, and experimental geometries. The first series was from a sandy bottom and the receiver was located at about 9.8 m from the sphere. In the second case the bottom was covered with a Mediterranean seagrass called Posidonia. The receiver was located approximately 6.0 m from the sphere in this case. Despite the different locations and somewhat different geometries, the experimental time series are very similar.

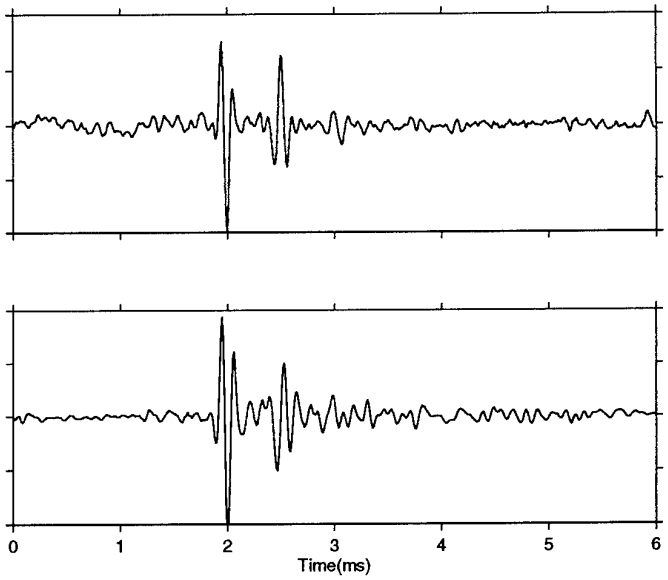

Figure 17: *Time series for scattering from aluminum sphere - different geometries and sites*

In Figs. 18 we show the experimental power spectrum of the backscattered signal (solid line) and the modelled spectra using a free space model in Fig. 18a and using the SSA in Fig. 18b. There is a slight improvement in the spectral amplitudes using the SSA. One noticeable feature in both Figs. 18a and 18b is the fact that the nulls predicted by the models are displaced from the experimental nulls. We have used an angle of incidence of 5° and a receiver angle of 3°. We note that for frequencies above about 13.0 kHz there is evidence of numerical oscillations in the model curves.

In Fig. 19, a comparison between the experimental and modelled time series is

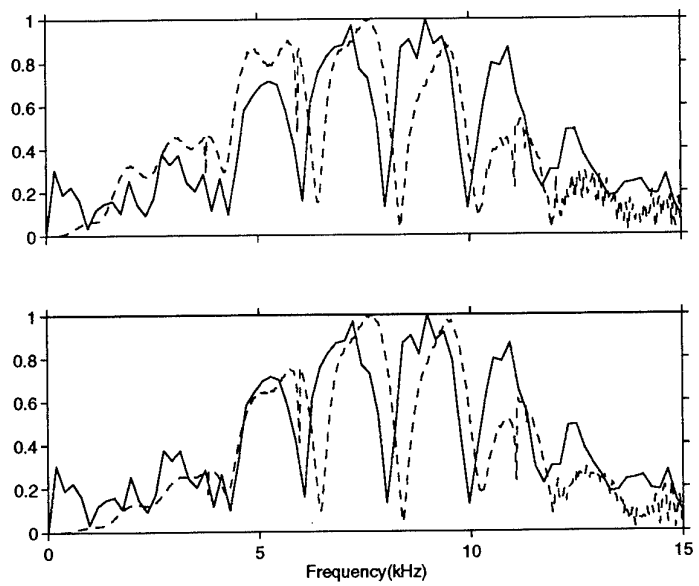

Figure 18: *Experimental (solid line) and modelled (dashed line) spectra using free space model and SSA for site 1*

shown using first a free-space scattering model and then using the single-scatter model. The experimental and modelled time series have been positioned in time by aligning the peak amplitude of the specular reflections. In the case of the free-space model the modelled time series seems to be almost 180° out of phase with the experimental series. In fact, the peak amplitude of the free-space series should probably be aligned with the the first positive peak of the experimental data (see Section 3 for more discussion of this point). The modelled time series using the single-scatter approximation is in very good agreement with the experimental data; however, it can be seen that the predicted Rayleigh wave arrival is slightly too fast. This is probably related to the null mismatch in the spectral domain.

We now repeat the analysis for the second site which is an area of the sea plant Posidonia. In Fig. 20 we show a comparison between the modelled and the experimental spectra. In this case, the nulls predicted by the models are even more displaced from the experimental nulls than for the previous site. Since the sphere is the same in both experiments, it would seem that either the geometry or the environment is affecting the spacing of these nulls although changing the geometrical inputs to the model did not significantly improve the agreement. In Fig. 21 we show the comparison between the experimental and modelled time series, first using a free-space model and in the lower graph the SSA. Once again, the SSA correctly predicts the specular reflected pulse, while the free space prediction appears to be almost 180° out of phase. It also predicts the Rayleigh pulse well in terms of shape but the arrival time is somewhat fast.

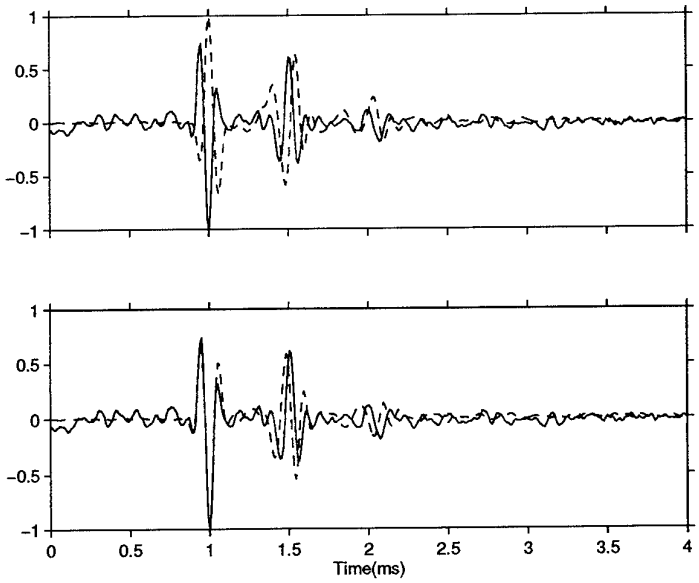

Figure 19: *Experimental and modelled (free-space and single-scatter model) time series for site 1*

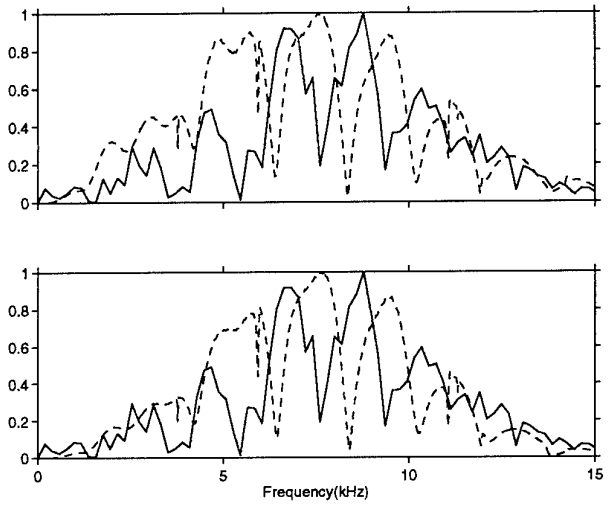

Figure 20: *Experimental (solid line) and modelled (dashed line) (free-space and single-scatter model) spectra for site 2*

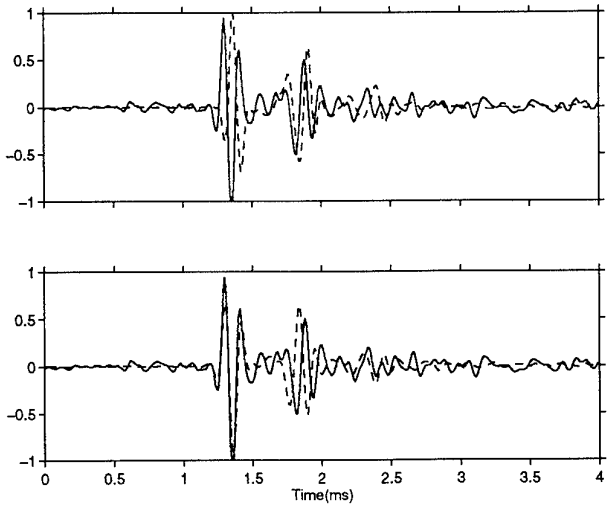

Figure 21: *Experimental (solid line) and modelled (dashed line) (free-space and single-scatter model) time series for site 2*

The SSA has done very well modelling the specular portion of the backscattered signal, but for this site even more than for the previous site, the SSA underestimates the arrival time of the Rayleigh pulse. Whether this is due to the inaccuracy of the SSA model for the circumferential energy, or whether it is some environmental effect (e.g., a slight settling of the sphere into the sediment, the presence of Posidonia, etc.) which is not correctly modelled, is not known. We can also improve the model results of the SSA by using a lower shear speed for aluminum (say 2900 or 3000 m/s) which effectively decreases the speed of the Rayleigh pulse.

In these figures we have aligned the modelled and experimental time series by aligning the absolute peak values. However, since the free space results and SSA results are computed identically (the free space result simply has no velocity or density jump at the interface) we can compare these series directly, which we do in Fig. 22. This emphasizes the previously discussed fact that the presence of the interface enlarges or diminishes certain features of the free-space specularly reflected pulse. The resulting pulse is not the negative version of the free-space pulse but only appears to be if one shifts the peak values in time by a small amount. The Rayleigh arrival looks quite similar for the two models and the relative arrival time of this pulse is the same in both cases.

Thus for the sphere we have seen that the SSA approximation does a very good job in predicting the shape of the specular reflection. The Rayleigh arrival is also correctly predicted in terms of shape, but the model predicts a slightly earlier arrival time than is seen in the experimental data. This discrepancy was more significant for the second site (Posidonia site) than for the first.

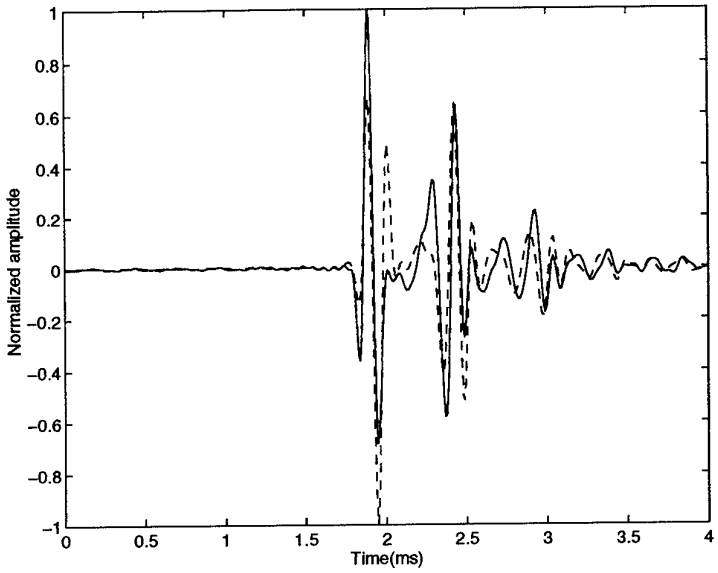

Figure 22: *Comparison of backscattered signal as computed by single-scatter model (hashed line) and free space model (solid line) with same time scale*

5 Summary

In this report, a single-scattering method has been used to model scattering from cylinders and spheres lying on a seabed. It was found that for shallow incidence and receiver angles, the amplitude and shape of the backscattered signal were significantly effected by the seabed. For these small angles, only a small velocity jump at the seabed is required to produce significant differences in the backscattered signal from the free space case. For larger impedance jumps, the backscattered signal is almost invariant to the sediment parameters.

We then modelled experimental data and had very good agreement. In the case of a water-filled cylindrical shell we showed good agreement with the entire signal. For a solid sphere we also had very good agreement in the time domain, although there was significant mismatch in the null-structure in the spectral domain. In particular, the shape of the specularly reflected pulse which appears to be the negative of the incident pulse (not a positive reflection as one would expect) is correctly predicted by the SSA model. However, the modelled arrival time for the Rayleigh pulse was a little too fast; this mismatch was larger for the second (Posidonia) site. The reasons for these mismatches are not known.

References

[1] F. Ingenito, "Scattering from an object in a stratified medium", J. Acoust. Soc. Am., **82**, pp. 2051–2059, 1996.

[2] M.D. Collins and M.F. Werby, "A parabolic equation model for scattering in the ocean", J. Acoust. Soc. Am., **85**, pp. 1895–1902, 1989.

[3] R. Lim, J.L. Lopes, R.H. Hackman, and D.G. Todoroff, "Scattering by objects buried in underwater sediments: Theory and experiment", J. Acoust. Soc. Am., **93**, pp. 1762–1783, 1993.

[4] J.A. Fawcett, "A plane-wave decomposition method for modeling scattering from objects and bathymetry in a waveguide", J. Acoust. Soc. Am., **100**, pp. 183–192, 1996.

[5] J.A. Fawcett, "Acoustic scattering from cylindrical objects embedded between two half-spaces", J. Acoust. Soc. Am., **100**, pp. 3053–3060, 1996.

[6] R. Lim, "Acoustic scattering by a partially buried three-dimensional elastic object", J. Acoust. Soc. Am., **99**, p. 2498, 1996.

[7] P. Gerstoft and H. Schmidt, "A boundary element approach to ocean seismoacoustic facet reverberation", J. Acoust. Soc. Am., **89**, pp. 1629–1642, 1991.

[8] J. Stratton, *Electromagnetic Theory*, McGraw-Hill Book Company, Inc, New York, 1941.

[9] N.D. Veksler, *Resonance acoustic spectroscopy*, Springer-Verlag, 1993.

[10] Bentech Subsea AS, *Simrad TOPAS PS 040 Operator Manual*

[11] W.L.J. Fox, J.A. Fawcett, D. Jourdain-Albonico, and A. Tesei, "Measurements of free-field acoustic scattering from cylindrical shells", SACLANTCEN Memorandum SM-331, 1997.

Document Data Sheet

NATO UNCLASSIFIED

Security Classification		Project No.
NATO UNCLASSIFIED		033-3
Document Serial No.	**Date of Issue**	**Total Pages**
SR-276	October 1997	30 pp.

Author(s)

Fawcett, J.A., Fox, W.L.J., Maguer, A.

Title

Modelling of scattering by objects on the seabed

Abstract

This paper describes some of the theory and implementation issues of modelling the backscattered energy from cylindrical or spherical objects lying on the seabed. The model utilizes a single-scatter approximation. The effects of various parameters such as grazing angle of the incident energy, receiver/scatterer geometry and the bottom halfspace geoacoustic parameters are investigated numerically. The paper is concluded with a comparison of modelled time series with experimental scattering data obtained for a steel-shelled cylinder and a solid aluminium sphere lying on a sandy seabed.

Keywords

Cylinder – sphere – seabed – scattering

Issuing Organization

North Atlantic Treaty Organization
SACLANT Undersea Research Centre
Viale San Bartolomeo 400, 19138 La Spezia, Italy

[From N. America: SACLANTCEN (New York) APO AE 09613]

Tel: +39 (0)187 540 111
Fax:+39 (0)187 524 600

E-mail: library@saclantc.nato.int

NATO UNCLASSIFIED

Initial Distribution for SR 276

Ministries of Defence

DND Canada	10
CHOD Denmark	8
DGA France	8
MOD Germany	15
HNDGS Greece	12
MARISTAT Italy	9
MOD (Navy) Netherlands	12
NDRE Norway	10
MOD Portugal	5
MDN Spain	2
TDKK and DNHO Turkey	5
MOD UK	20
ONR USA	42

NATO Commands and Agencies

NAMILCOM	2
SACLANT	3
CINCEASTLANT/ COMNAVNORTHWEST	1
CINCIBERLANT	1
CINCWESTLANT	1
COMASWSTRIKFOR	1
COMMAIREASTLANT	1
COMSTRIKFLTANT	1
COMSUBACLANT	1
SACLANTREPEUR	1
SACEUR	2
CINCNORTHWEST	1
CINCSOUTH	1
COMEDCENT	1
COMMARAIRMED	1
COMNAVSOUTH	1
COMSTRIKFORSOUTH	1
COMSUBMED	1
NC3A	1
PAT	1

Scientific Committee of National Representatives

SCNR Belgium	1
SCNR Canada	1
SCNR Denmark	1
SCNR Germany	1
SCNR Greece	1
SCNR Italy	1
SCNR Netherlands	2
SCNR Norway	1
SCNR Portugal	1
SCNR Spain	1
SCNR Turkey	1
SCNR UK	1
SCNR USA	2
French Delegate	1
SECGEN Rep. SCNR	1
NAMILCOM Rep. SCNR	1

National Liaison Officers

NLO Canada	1
NLO Denmark	1
NLO Germany	1
NLO Italy	1
NLO Netherlands	1
NLO Spain	1
NLO UK	1
NLO USA	1

Sub-total	208
SACLANTCEN	30
Total	238